Laser Generation of Iron-Doped Silver Nanotruffles with Magnetic and Plasmonic Properties

Vincenzo Amendola,[a,*] Stefano Scaramuzza,[a] Stefano Agnoli,[a] Gaetano Granozzi,[a] Moreno Meneghetti,[a] Giulio Campo,[b] Valentina Bonanni,[b] Francesco Pineider,[b] Claudio Sangregorio,[b,c] Paolo Ghigna,[d] Stefano Polizzi,[e] Piero Riello,[e] Stefania Fiameni,[f] Luca Nodari[f]

[a] Department of Chemical Sciences, Università di Padova, via Marzolo 1, I-35131 Padova, Italy
[b] Department of Chemistry, University of Florence & INSTM, I-50019 Florence, Italy
[c] ICCOM-CNR, Sesto Fiorentino, I-50019 Florence, Italy
[d] Department of Chemistry, Università di Pavia, Viale Taremelli 13, I-27100, Pavia, Italy
[e] Department of Molecular Sciences and Nanosystems, Università Ca’ Foscari Venezia and INSTM UdR Venezia, via Torino 155/b, I-30172 Venezia-Mestre, Italy
[f] CNR – IENI, Corso Stati Uniti, 4 35127 Padova, Italy

** Corresponding author: vincenzo.amendola@unipd.it*

Abstract

A frontier topic in nanotechnology is the realization of multifunctional nanoparticles (NPs) by the appropriate combination of different elements of the periodic table. The coexistence of iron and silver in the same nanostructure, for instance, is interesting for nanophotonics, nanomedicine and catalysis. However, alloying of Fe and Ag is inhibited for thermodynamic reasons. Here it is described the synthesis of Fe-doped Ag NPs bypassing thermodynamics constraints by laser ablation in liquid solution. These NPs have an innovative structure consisting in a scaffold of face centred cubic metal silver alternating with disordered Ag - Fe alloy domains, all arranged in a truffle-like morphology. Fe-Ag NPs show the plasmonic properties of silver and the magnetic response of iron-containing phases, and the surface of Fe-Ag NPs can be functionalized in one step with thiolated molecules. Taking advantage of the multiple properties of Fe-Ag NPs, magnetophoretic amplification of plasmonic properties is demonstrated with proof-of-concept experiments of surface enhanced Raman scattering (SERS) and photothermal heating. The synthetic approach is of general applicability and virtually permits the preparation in one step of a large variety of multi-element NPs.

Keywords: Silver Nanoparticles, Iron Nanoparticles, Laser Ablation, Nanoalloys.

Table of contents entry

Nanoparticles with truffle-like shape, composed of the two thermodynamically immiscible elements Fe and Ag, are obtained by laser ablation in liquid. The Fe-doped Ag nanotruffles are capable of magnetophoretic amplification of plasmonic properties, such as SERS and photothermal heating.

ToC figure

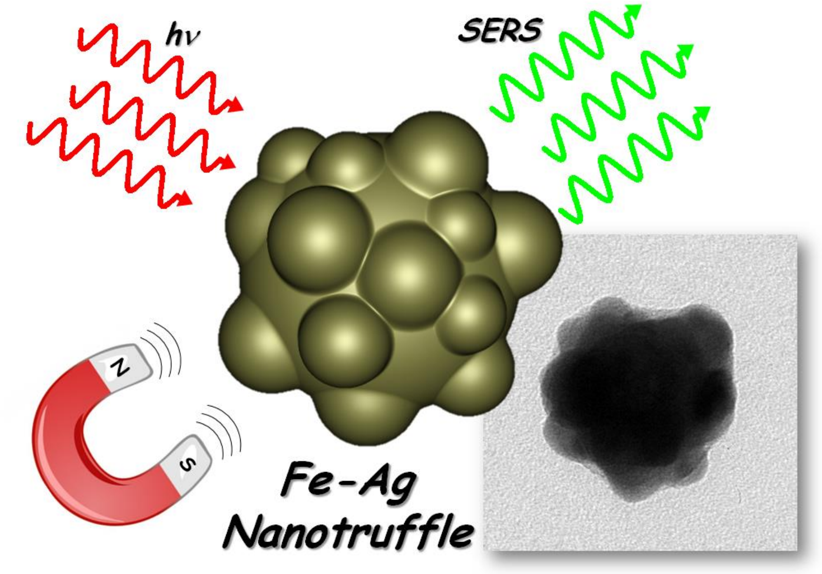

Introduction.

The frontier of nanotechnology is continuously progressing towards the realization of multifunctional nanoparticles (NPs), in which different properties are achieved by a fine control of nanomaterials structure and composition.[1-3] The addition of distinct elements in the same nanometric "box" is a successful strategy to expand the range of physical-chemical properties available within a single nanotool, and sometimes it allows the discovery of new phenomena and of synergistic performances.[4-9] In particular in the case of plasmonic materials, this concept recently opened the way to the realization of multielement NPs in the form of alloys or heterostructures, where a noble metal with excellent plasmonic response, such as gold and silver, coexists with a metal with magnetic or catalytic properties such as transition metals (Fe, Co, Ni, Ti, Rh) or other "non-plasmonic" noble metals (Pt, Pd).[5-7, 10] In several cases, mutual interactions between the distinct physical-chemical properties of each element are observed, a feature that is highly desirable in fields such as magneto-plasmonics,[11-13] and plasmon enhanced catalysis.[14] The potential application range for these multi-element particles is wide, covering for instance the realization of multimodal contrast agents for nanomedicine,[15] selective cargos for drug delivery,[16] theranostic particles,[17] light-triggered antibacterial materials,[18, 19] devices for magneto-optical information processing,[20] new catalysts activated by the sunlight,[21] magnetically recoverable catalysts,[22, 23] efficient nanosensors,[24, 25] or SERS substrates.[26, 27]

The realization of a nanoalloy is a straightforward approach to achieve multifunctional nanomaterials whenever the desired elements can be mixed in a single phase in ordinary reaction conditions, either for thermodynamic or kinetic reasons.[6, 28, 29] When mixing at the nanoscale is not possible, instead, the synthetic strategy proceeds by formation of heterostructures, usually with a multistep process where the crucial role is played by the wettability of the phases containing the two elements.[6, 7, 30]

Alternatively, one can attempt out-of-equilibrium synthetic approaches to place immiscible elements inside the same nanostructure.[28] Laser ablation synthesis in solution (LASiS) is such an example, since it operates in conditions where the kinetics of NPs formation is very fast and, often, the final phase of the products is not the thermodynamically favoured one.[31, 32] In LASiS, a bulk target is immersed in a liquid solution and it is ablated by focused laser pulses.[32] The NPs, which can form either by nucleation and growth of ablated vapours or by solidification of melted drops ejected from the target, are collected as a colloidal solution directly in the liquid.[32] We recently demonstrated the potential of LASiS for the preparation of magnetic-plasmonic Fe-Au nanoalloys with a composition exceeding the room temperature thermodynamic limit.[33, 34] In fact, Fe-Au NPs with same phase and composition had never been obtained before as colloidal solutions by standard synthetic approaches such as the wet chemistry methods.[33] LASiS exploited in particular the fact that kinetically stable bulk Fe-Au alloys can be obtained at room temperature and pressure by melting and fast cooling,[32] thus permitting the transfer of the target phase from the bulk scale to the nanoscale through the fast kinetics of the laser ablation process.

Another attractive example of magnetic-plasmonic material is represented by the Fe-Ag system, since silver has superior plasmonic performances than gold.[6, 7, 35] Contrary to Fe-Au, however, Fe and Ag do not form thermodynamically stable alloys at any temperature.[36, 37] Moreover, kinetically stable Fe-Ag ordered alloys, where iron is present as a substitutional impurity in the face centred cubic (fcc) lattice of silver, or silver replaces iron in its body centred cubic (bcc) lattice, have never been observed in the bulk phase.[36-39] Consequently, the sole examples of bimetallic Fe-Ag nanometric particles consist in the non plasmonic $AgFeO_2$ oxide,[40] or in heterostructures where the plasmonic Ag phase and the magnetic Fe phase (either metal or oxides) are grown during distinct synthetic steps.[7, 41, 42]

Here we exploited the LASiS to obtain in a single step magnetic-plasmonic Fe-Ag NPs. Composition, structure and shape of NPs retain the traces of the fast kinetics of particles formation, and this allowed the inclusion of magnetic and plasmonic phases within the same nanometric object. The surface of Fe-Ag NPs can be functionalized in one step with thiolated molecules, by formation of sulphur-silver chemical bonds, thus enabling another degree of freedom to improve their properties. The multifunctionality of Fe-Ag NPs opens the way to a series of applications and, for instance, we demonstrate that magnetic amplification of the plasmonic properties such as surface enhanced Raman scattering (SERS) or photothermal heating is possible with our systems.

In general, our results demonstrate that LASiS can be a general approach for the preparation in one step of multielement NPs, bypassing the thermodynamic limitations to miscibility and, thus, providing an innovative and versatile method to access a wide range of new multifunctional nanostructures.

Results.

Synthesis and characterization.

Fe-Ag NPs were obtained by LASiS with near infrared (1064 nm) pulses (Figure 1a), starting from a bulk bimetallic target with composition 34at% of metal Fe and 66at% of metal Ag, as measured by energy dispersive X-ray spectroscopy (EDS) and Rietveld analysis of the X-ray diffraction (XRD) pattern. In particular, the Rietveld analysis of bulk target XRD pattern (see Figure S1 of E.S.M.) clearly indicated that metal iron is in the bcc structure with average grain size of 34 nm, and metal silver is in the fcc structure with average grain size of 71 nm, while no traces of alloying between Fe and Ag were detected. The laser ablation was performed in ethanol, which is a Class 3 and environmentally friendly liquid, thus contributing to make the overall synthetic procedure compatible with the principles of “green” chemistry.[43] Besides, we selected ethanol because it was previously used for the LASiS of silver[32, 44] or iron-containing[32, 45] NPs.

Laser generated Fe-Ag NPs were mixed with a solution of thiolated polyethylene glycol (PEG) and EDTA, kept at 30°C for 1 hour, dialysed and finally resuspended in distilled water. Finally, the magnetic fraction of nanoparticles (fraction M) was separated from the non-magnetic fraction (fraction NM) in the following way: fraction M was focused on the bottom of an eppendorf tube by applying an external magnetic field, then the supernatant (fraction NM) was removed by a micropipette and, finally, fraction M was resuspended in distilled water for further manipulation. In fact, thiolated PEG can chemically bind the surface of Fe-Ag NPs, by the formation of sulphur-silver chemical bonds,[46] providing stability to the colloidal system in several polar and non polar liquids. EDTA is required to remove synthesis by-products like amorphous/crystalline iron oxides and hydroxides, as usually done with iron-based NPs obtained by LASiS.[33, 47] In this way, only the PEG-coated NPs remains in solution after the dialysis step by centrifugation in 10 kDa concentration membranes. The effective coating with PEG, assessed by Fourier transformed infra-red (FTIR) spectroscopy, is immediately appreciable by the yellow colour of the Fe-Ag NPs solution, which actually is typical of colloidal silver[35, 46] (Figure 1b). In fact, the optical absorption spectrum of the Fe-Ag NPs solution shows a sharp peak at about 430 nm, due to the surface plasmon resonance (SPR) of silver[35, 46] (Figure 1c-d). The optical properties of Fe-Ag NPs do not change even several weeks after their preparation, thus assessing the stability in time and in aqueous solution of our nanomaterials.

Importantly, the presence of the SPR in the magnetically responsive phase (Figure 1c-d) is a clear indication that the plasmonic silver phase coexists with the magnetic iron phase.

The comparison of the optical absorption spectra of the different Fe-Ag NPs fractions gives useful information about synthesis products. Compared to the NM fraction, the SPR of “magnetic” Fe-Ag NPs is broader and red shifted of ~25 nm, which is compatible with the presence of particles with size larger than ~50 nm or with non-spherical shape,[35, 48, 49] whereas the sharp plasmon band at 400nm observed in the NM fraction is typical of spherical Ag NPs with size below ~50 nm.

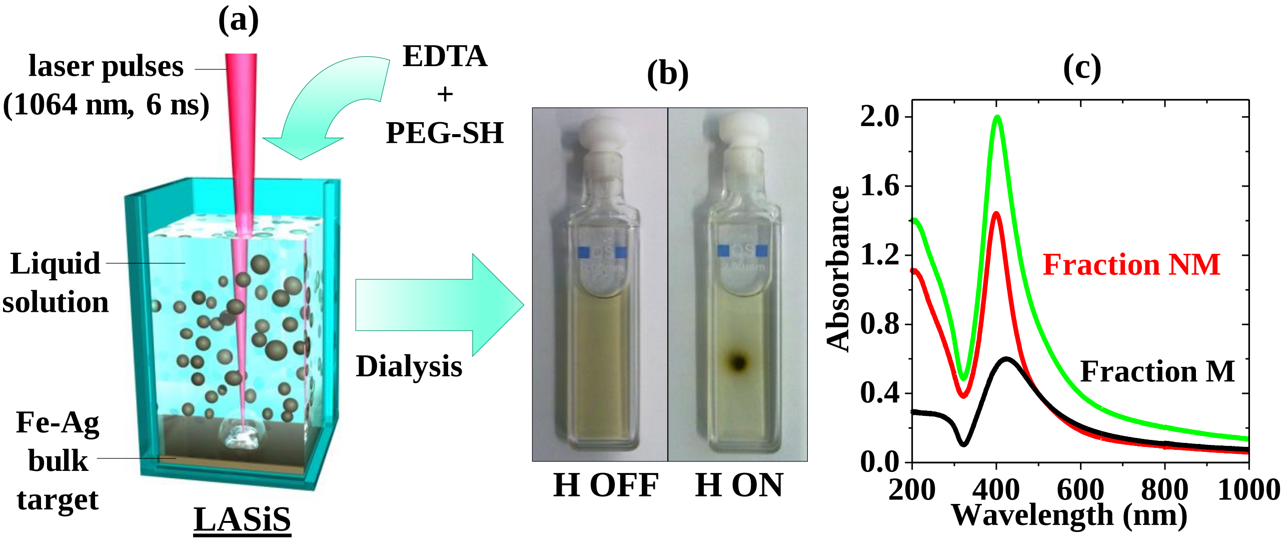

Figure 1. Sketch of LASiS (a) and pictures (b) of Fe-Ag NPs solution showing the yellow-green colour typical of plasmonic silver and the accumulation of NPs by the magnetic field H, applied by placing a small NdFeB magnet on one side of the cuvette. (c) OAS spectra of PEG-coated Fe-Ag NPs synthesized in ethanol and redispersed in water just after the synthesis (green line), and after the magnetic sorting in fractions M (magnetic, red line) and NM (non-magnetic, black line).

In order to obtain structural information at the level of the single NP, Fe-Ag NPs were investigated by transmission electron microscopy (TEM). The sample is composed by relatively large NPs (Figure 2a), with a size distribution peaked at ~90 nm. Interestingly, NPs in fraction NM are smaller (Figure 2b) and the size distribution is bimodal (Figure 2c), with a peak due to small NPs centred at ~5nm and a broad population of large NPs ranging from 10 to 50 nm. In addition, a remarkable morphological difference exists between NPs in the two fractions: in fraction M, NPs have a truffle-like structure since they appear as the agglomeration of smaller clusters partially fused together, originating particles with irregular surfaces (Figure 2a), whereas NPs in fraction NM are mostly spherical, with a minority of spheroidal shapes (Figure 2b). By numerical calculations of the optical properties of silver NPs with spherical or truffle-like structure, reported in Figure 2d, we assessed that the difference of size and shape are compatible with the different optical properties of M and NM fractions, reported in Figure 1c. In particular, although the morphological complexity of real samples cannot be reproduced just by a simplified model, numerical calculations in Figure 2d show that a broader and red shifted SPR is compatible with truffle-like silver NPs with structure similar to that reported in Figure 2a, whereas a sharp SPR at 400 nm is compatible with spherical NPs such as those in Figure 2b.[35]

In all Fe-Ag NPs of fraction M, both Ag Lα (3.0 keV) and Fe Kα (6.4 keV) peaks are found by EDS (Figure 2e). This was further substantiated by line scan EDS mapping on a cluster of NPs (Figure 2f), showing that Fe Kα and Ag Lα signals are overlapped. In particles of fraction NM, instead, the Ag signal was the only one detected, with a few exceptions (~5%) corresponding to >50nm NPs, where weak iron peaks were found together with a largely dominating silver signal. This clearly explains the different magnetic response of NPs in the M and NM fractions: since the attractive magnetic force scales with the mass of the magnetic material,[50] those NPs with negligible content of iron or with small size were not attracted by the magnetic field, contrary to those NPs where an appreciable amount of iron coexists with silver.

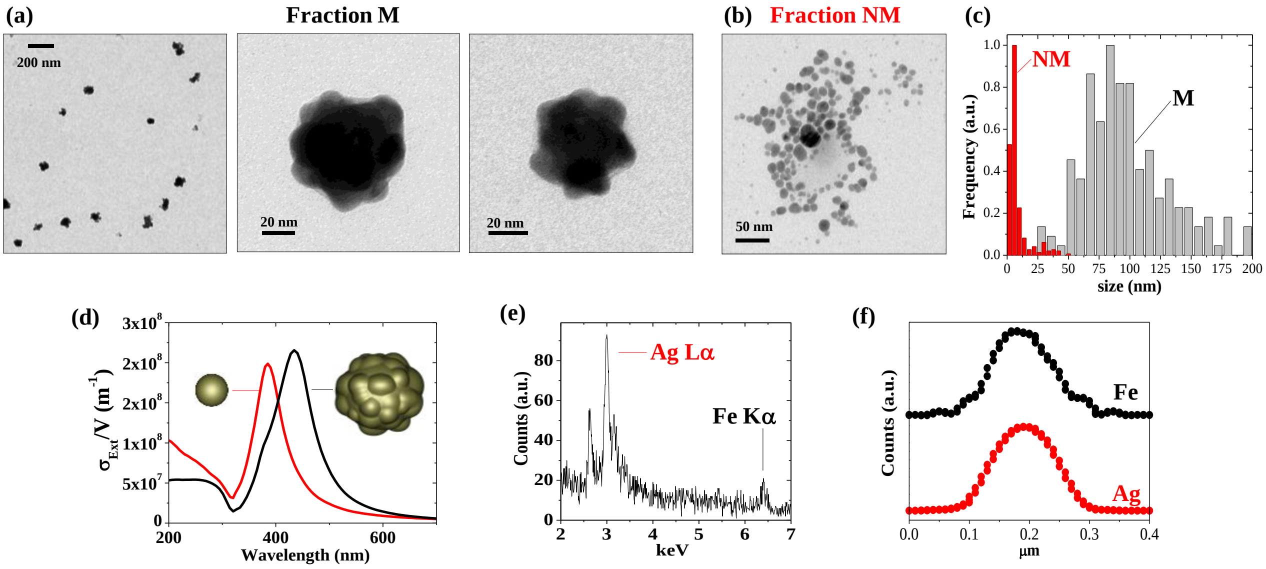

Figure 2. Representative TEM images of Fe-Ag NPs in fraction M (a) and NM (b), and size histograms (c). (d) Numerical simulation of the extinction cross section of a spherical Ag NP with size of 5 nm, representative of nanoparticles in (b), and of an Ag nanotruffle with structure and size representative of nanoparticles in (a). In both cases, we considered a water matrix. (e-f) Representative EDS spectrum (e) and line scan intensity (f) of the Ag L lines and Fe K lines collected on Fe-Ag NPs from fraction M.

The iron content in the Fe-Ag NPs of fraction M was quantitatively assessed by inductively coupled plasma assisted mass spectrometry (ICP-MS) and resulted of 15at%, which is lower than the bulk target content (Fe 34at%). This means that part of Fe was removed during the purification/dialysis step, in agreement with our previous observation about the LASiS of Fe-Au NPs.[33, 34, 51]

The chemical composition of Fe-Ag NPs (fraction M) was further investigated by x-ray photoelectron spectroscopy (XPS), revealing the presence of sulphur, carbon, silver, oxygen and iron photoemission lines. Sulphur *2p* (Figure S2a in E.S.M.) and carbon *1s* (Figure S2b in E.S.M.) peaks are due to the shell of thiolated ligands surrounding the NPs, further confirming the coating of Fe-Ag NPs with the organic stabilizing layer. The photoemission line of Ag ($3d_{5/2}$ peak, Figure 3a) has a main chemical component centred at a BE of 368.4 eV, which is the typical Ag(0) value expected for plasmonic silver.[52] The Fe 2*p* photoemission spectrum, reported in Figure 3b, is constituted by several different components with a complex multiplet structure. Although the identification of a prevailing component is not possible, the Fe $2p_{3/2}$ peak is located at the BE typical of oxides (709-714 eV), with a tail at values often observed in alloys between metal iron and other noble metals (708 eV).[34, 53-55] In order to probe the chemical nature of the Fe-Ag NPs below the embedding layer of PEG molecules, the sample was sputtered for 10’ with Ar^+ (1 keV), after that we observed the increase of the silver and iron components and a concomitant strong decrease of the carbon signal, due to the erosion of the ligand shell. Importantly, a shoulder appears at 707-708 eV in the iron signal (red line in Figure 3b), which is the value typical of metal iron.[56] Therefore, iron at the surface of the Fe-Ag NPs is almost completely oxidised, whereas a mixture of metal and oxidized iron is present inside the particles. The surface layer of oxide is useful for the passivation of Fe-Ag NPs, and it explains the persistence of Fe(0) for several weeks after synthesis in aqueous solution, as recently found also for Fe-Au nanoalloys obtained by LASiS.[34]

The presence of a complex multiplet structure in the photoemission spectrum of Fe suggests that iron phases are disordered and there is not a dominating crystalline phase. Hence, we performed XRD analysis on the “magnetic” Fe-Ag NPs to obtain more information about sample’s crystallinity. The XRD pattern (Figure 3c) clearly shows all the peaks of fcc silver, but no reflections ascribable to iron phases are found. This marks a remarkable difference with the XRD pattern of the target used for laser ablation, where the reflections of both metal Ag (fcc) and Fe (bcc) are present (see Figure S1 in E.S.M.). The content of Fe in the Fe-Ag NPs measured by ICP-MS and EDS is about 15 times the XRD detection limit of crystalline iron phases with size larger than ~5-3 nm in our experimental conditions. In agreement with XRD, also Raman and FTIR spectroscopic analysis on Fe-Ag NPs excluded the presence of iron oxides with large (e.g. >5-10nm) crystalline grains. Therefore, our results recall previous studies in thin Fe-Ag films[57, 58] where the iron-containing phase is disordered or organized in ordered domains with extremely small size, i.e. with high defectivity due to the large surface-to-volume ratio.

Even in the case of heterogeneous or amorphous samples, Mössbauer spectroscopy can provide valuable information about the chemical environment and the crystalline order around Fe atoms.[36] The spectrum of the Fe-Ag NPs, reported in Figure 3d, reflects the structural complexity suggested by the previous characterization techniques, being dominated by an intense absorption close to 0 mm/s and by a broad magnetically splitted component. The best fitting was obtained by means of three components (see Table S1 in E.S.M. for details), therefore, the spectrum describes three different types of environment for the Fe atoms in Fe-Ag NPs: *i*) 40% of superparamagnetic Fe atoms in a metal iron bcc lattice with small grain size (at least below 10 nm), *ii*) 30% of paramagnetic Fe atoms in sites characterized by the absence of magnetic coupling, which are compatible with an environment composed only of Ag atoms and *iii*) 60% of Fe atoms in two different sites showing magnetic coupling, which are compatible with a mixed environment of Ag and Fe atoms.

In agreement with all the previous characterization techniques, the Mössbauer spectrum does not indicate the presence of ordered iron oxide crystalline domains with concentration large enough to be detected. This means that surface iron oxide is prevalently amorphous and do not give a clearly identifiable contribution to of the total iron signal in our sample, likely contributing to the background of the Mössbauer spectrum.

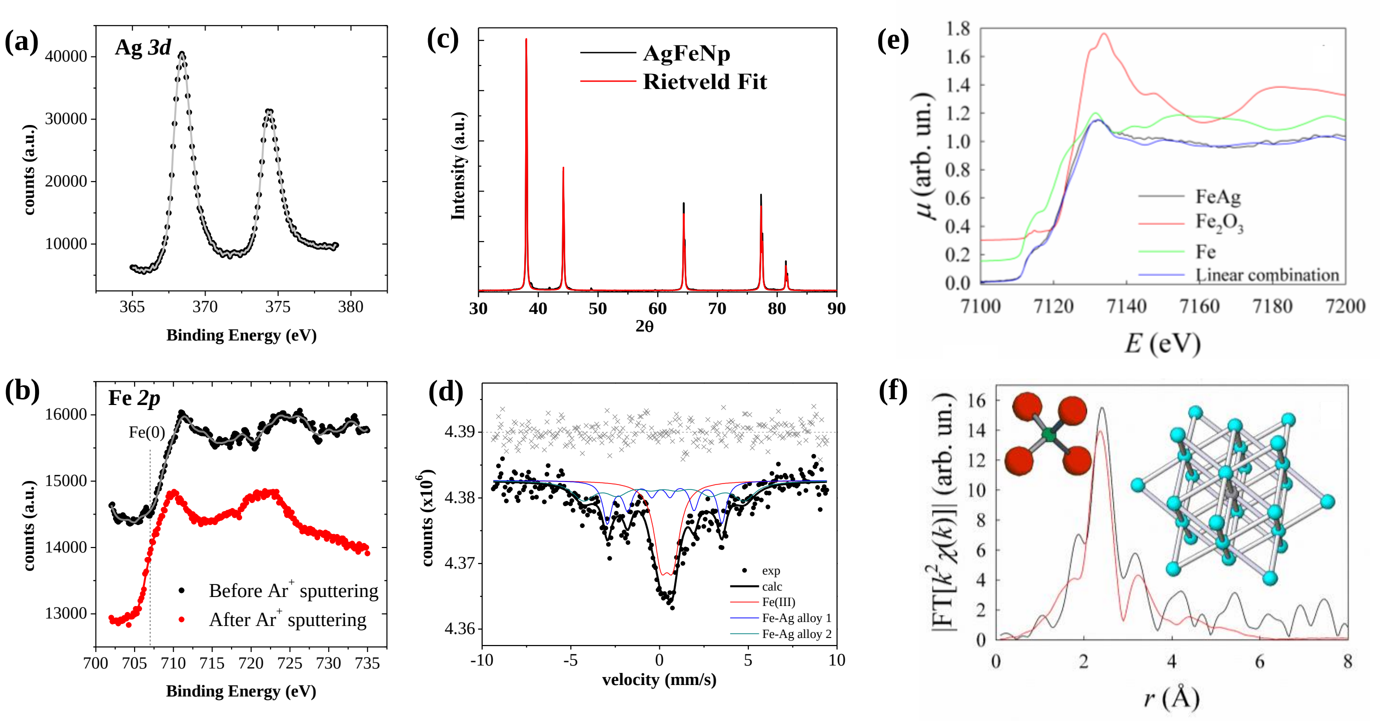

Figure 3. (a-b) X-ray photoemission Ag 3d (a) and Fe 2p (b) peaks. (c) XRD pattern of the Fe-Ag NPs of fraction M (black line) and relative Rietveld fit (red line). (d) Mössbauer spectrum of the Fe-Ag NPs fitted with four components (for details see text). Grey crosses are fit residuals. (e) XANES Fe-K edge spectrum of the sample investigated in this work. The spectra of bulk metallic Fe and of an Fe oxide (Fe_2O_3) are also shown for better reference; for the sake of clarity the spectra have been shifted along the *y* axis. (f) EXAFS Fourier transformed modulus, its fit (red line) according to the model of Table S2 in E.S.M., and the two clusters used in the fit (green: Fe(III); gray: Fe(0), cyan: mixed Fe/Ag (50/50); red: oxide ions).

The actual crystal structure of the Fe-Ag NPs (i.e. bcc-like or fcc-like), that cannot be discriminated by room temperature Mössbauer spectroscopy, was further investigated by X-ray Absorption Spectroscopy (XAS). Figure 3a shows the x-ray absorption near edge structure (XANES), where the edge energy position and shape are strongly dependent on the electron count and structure on the photoabsorber and, in particular, the edge shifts at higher energy with increasing of its oxidation state. Comparison with the XANES of a metallic Fe foil and of Fe_2O_3 shows the presence of Fe in the Fe(0) oxidation state. In addition, in the pre-edge region, where the $1s \rightarrow 3d$ transitions are located, the clear appearance of a Fermi level demonstrates that Fe is present in the metallic state. However, the XAS spectrum of this sample shows remarkable differences with respect to that of bulk metallic Fe. In particular, the edge appears to be slightly shifted towards higher binding energies if compared to that of metallic Fe, indicating that a fraction of Fe should be present in a more oxidised state.

Actually, a linear combination of the spectra of Fe_2O_3 and Fe, shown in the figure as a blue line, with a weight of Fe equal to 70 %, gives a good agreement with the edge position of the sample.

In addition, the XANES and the extended x-ray absorption fine structure (EXAFS, see Figure S3a in E.S.M.) oscillations after the edge are much dumped when compared to bulk metallic Fe, which is a clear indication that the local atomic environment of Fe is disordered. According to the XANES analysis, the Fourier Transforms of the Fe-Ag NPs EXAFS spectra (see Figure 3f and S3b in E.S.M.) have been fitted with a model containing two clusters, one accounting for a disordered Fe(III) oxide and weighting for 30 %, and the other one accounting for a disordered Fe/Ag alloy, derived form the bcc structure of Fe (structural parameters are reported in Table S2 in E.S.M.). The best agreement with the experiment (shown as a red line in Figure 3f and Figure S3b of E.S.M.) was obtained when the Ag atoms are present as random substituents of Fe atoms in the Fe/Ag alloy with bcc structure, with Ag/Fe ratio of ca. 50:50, and the Fe(III) oxide contains fourfold coordinated Fe (the cluster used in the fit are shown in Figure 3f).

The quite large values for the EXAFS Debye-Waller factors for all the coordination shells confirms the overall disordered structure around Fe atoms in the NPs. Nonetheless, we found an EXAFS goodness of fit (GOF) of 30%, which, considering the unavoidable noise level in the spectrum, points to a fair agreement between experiment and structural model.

Since the Fe-Ag NPs are responsive to the application of an external magnetic field and structural analysis evidenced the presence of metallic Fe and disordered Ag-Fe phases, the sample of fraction M was investigated quantitatively by SQUID magnetometry. The hysteresis loop collected at room temperature (Figure 4a) is almost fully reversible and the magnetization, at the highest measuring field, is 33 Am^2/kg of iron. Conversely, at low temperature (2.5 K) the loop is open with a coercive field of 28 mT, a reduced remnant magnetization of 0.11 and a saturation magnetization, extrapolated from high field data of ca. 50 Am^2/kg (see Figure S4 in E.S.M. for a better view of the low-field part of hysteresis loop). The observed behaviour is consistent with the presence of single domain magnetic nanoparticles, whose magnetic moments are blocked at low temperature and enter the superparamagnetic state at room temperature.[59] The temperature dependence of the Zero Field Cooled and Field Cooled magnetizations (Figure 4b) well supports this conclusion. Interestingly, the hysteresis loop at 2.5 K does not saturate at the lowest measuring temperature, indicating that a fraction of weakly coupled/disordered magnetic moments occurs in the sample. The presence of this component is better evidenced by the marked decrease with temperature of the magnetization measured at 5 T, (ca. 12% decrease from 2.5 to 20 K, shown in Figure S5 in E.S.M.). The saturation magnetization measured at 2.5 K corresponds to 0.5 μ_B per iron atom, a value lower than that expected for ferromagnetically coupled Fe atoms. However, it should be taken into account that finite size effects on one hand and the presence of spin disorder and of a certain amount of amorphous iron oxide on the other, can concur to strongly decrease the total magnetization. In particular, the presence of surface layer of iron oxide, already evidenced by XPS and XAS experiments, is indirectly confirmed by the shift of the hysteresis loops along the field axis observed after the sample was cooled in a 5 T magnetic field (see Figure S4 in E.S.M.). This behavior is the typical signature of exchange bias generated by the presence of an interface such as that of metal/metal oxide core/shell nanostructures.

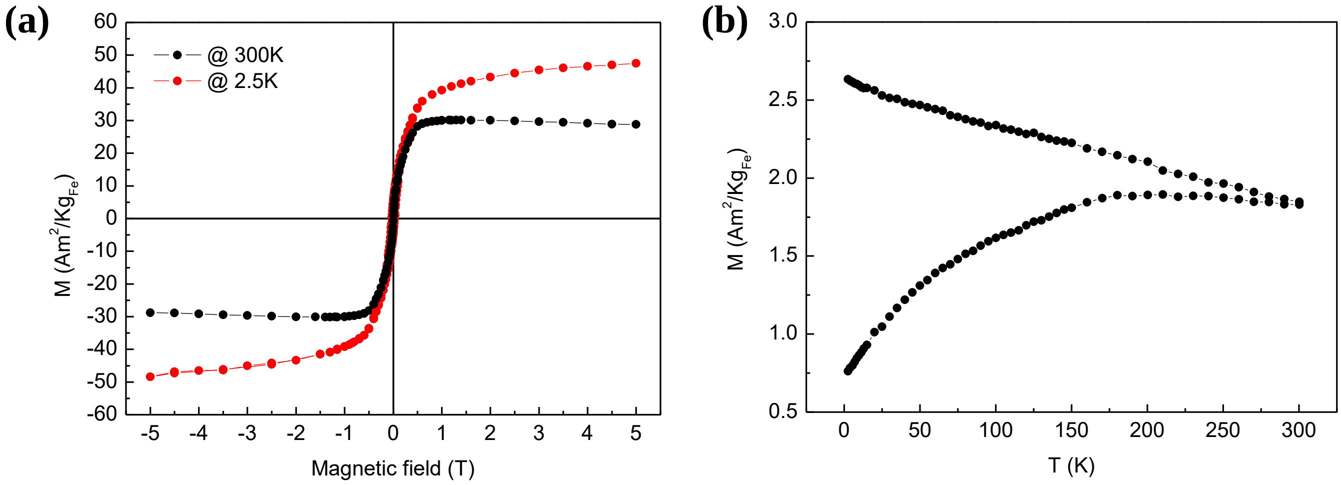

Figure 4. Magnetic characterization of Fe-Ag NPs in fraction M. (a) Hysteresis loops collected at 300 K and 2.5 K. (b) temperature dependence of the ZFC-FC magnetization measured with a 5 mT probe field.

Magnetophoretic amplification of plasmonic response.

Since we obtained a multifunctional nanomaterial endowed with magnetic and plasmonic properties and a complete colloidal stability, we used all these features in a synergistic way to amplify the plasmonic response in a localized area by magnetophoretic accumulation for practical applications such as SERS and photothermal heating.

Magnetic amplification of SERS with Fe-Ag NPs was investigated at 633 nm with a micro-Raman spectrometer, by adding a cationic dye (malachite green, MG) to the particles dispersion. In this experiment, SERS measurements were performed before (H=0) and after (H>0) the application of a small (∅=2 mm) NdFeB magnet in the point of analysis. In this way, the Fe-Ag NPs were reversibly focused by the external magnetic field on an area as small as the face of the magnet. MG is a cationic molecule which can interact with negatively charged NPs, which is well suited for the present case because we have found by Z-spectroscopy that the Fe-Ag NPs have a negative Z-potential of -26±5 mV. Being Fe-Ag NPs coated with PEG, the addition of the cationic analyte does not induce the coagulation of the colloid, which instead remains stable.

As shown in Figure 5a, the Raman spectrum collected on the quartz cuvette containing the Fe-Ag NPs mixed with MG is 10 times more intense after magnetic focusing, allowing the detection of a bright signal at analyte concentration as low as $8 \cdot 10^{-8}$ M (ca. 40 picomols of analyte), which is the same order of magnitude reported in literature for similar experiments.[26, 27]

Magnetic amplification of photothermal heating with Fe-Ag NPs was investigated by 785 nm continuous wave (CW) laser irradiation. Similar to the SERS experiment, photothermal measurements were performed before (H=0) and after (H>0) the application of a NdFeB magnet in the point of laser irradiation (see Figure 5b). In this way, the Fe-Ag NPs were efficiently accumulated in a small area equivalent to the millimetric laser spot size, with the effect of increasing the rate of light-to-heat conversion, as shown by thermal imaging of the sample (Figure 5b). Conversely, the concentration of absorbing centers in the laser spot is lower in the absence of magnetic accumulation, resulting in a lower sample heating.

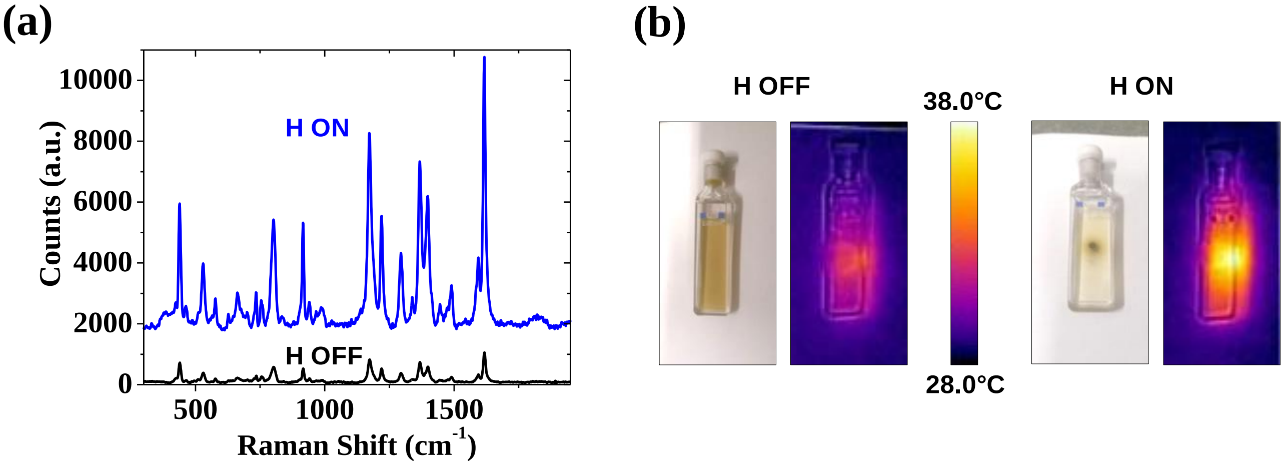

Figure 5. (a) Raman spectra of the MG/Fe-Ag NPs dispersion before (H=0, black line) and after (H>0, blue line) magnetic focusing. The blue spectrum is vertically shifted for clarity. (b) Photothermal heating experiment by cw laser irradiation at 785 nm of the Fe-Ag NPs dispersion before (H=0, black line) and after (H>0, blue line) magnetic focusing.

Discussion

Phase of Fe-Ag nanotruffles. Our structural investigations confirmed that NPs of fraction “M” are actually composed of two immiscible elements, i.e. silver and iron. In particular, XRD and SAED identified crystalline fcc silver as the dominating ordered phase, whereas TEM, Mössbauer and EXAFS revealed that metal iron is mostly present in disordered Fe-Ag alloy domains, which are not detectable by XRD. However, iron atoms located at the surface of NPs inevitably undergo oxidation, as assessed by XPS. The Fe-Ag NPs are superparamagnetic at room temperature, and we exploited the coexistence of magnetic and plasmonic properties for the amplification of SERS and photothermal performances in well localized regions by using a small commercial NdFeB magnet.

According to the Fe-Ag phase diagram, the two metals are immiscible both in the solid and in the liquid phase.[36] Contrary to other cases of bimetallic compounds, which can be obtained as kinetically stable ordered alloys despite the unfavourable thermodynamics,[15, 33, 60] the Fe-Ag system only form disordered alloys, even when out-of-equilibrium synthetic approaches such as sputtering are used.[36-38, 58] At the nanoscale, silver nanocrystals with size larger than ~5 nm have the same structural constraints of bulk or thin film equivalents,[61, 62] therefore the same miscibility limitations of the bulk Fe-Ag system is valid for Fe-Ag NPs. Recently, Peng et al. reported an experimental and theoretical investigation on the nucleation of a new thermodynamically favoured crystalline phase from another crystalline phase with unfavourable thermodynamics.[63] This process takes place in conditions of limited atomic mobility due to the solid crystalline environment. Their results showed that a disordered (liquid like) structure can form when the interfacial free energy with surrounding crystalline phases is lower than with the other thermodynamically allowed ordered phases.[63] Therefore, the formation of disordered Fe-Ag domains instead of distinct crystalline Fe and Ag nanocrystals is possible during the rapid cooling of NPs generated by LASiS if *i)* atomic mobility is limited and *ii)* the formation of new interfaces between ordered metals has higher energetic cost compared to the arrangement of metal atoms in a disordered Fe-Ag structure.

Morphology of Fe-Ag nanotruffles. The morphology and the chemical composition of our Fe-Ag NPs retains the traces of the fast kinetics of formation occurring with LASiS. In LASiS, the laser pulses focused on the bulk target extract matter by generation of a plasma plume, on a time scale of few ps, which expands in the liquid buffer over a time of hundreds of ns, releasing heat to the surrounding solution and forming a cavitation bubble that expands and collapses on a timescale of hundreds of microseconds.[32] The exact mechanism of NPs formation is still object of intense theoretical and experimental investigations,[32, 64] and it is highly dependent on the system parameters such as the laser pulse duration and energy.[32] However, there is a large number of evidences that nanomaterials obtained by LASiS form by coalescence of smaller crystalline nuclei with nanometric size.[32] These nuclei can be extracted directly from the target, or can form by nucleation of atomic and molecular vapours present in the plasma plume.[32] In the case of a target composed of a single element (such as pure Ag)[46] or miscible elements (such as Ag and Au),[65, 66] the coalescence of pristine nuclei generates spherical or rounded NPs, due to the high temperature in the LASiS environment and the consequent high mobility of atomic species on the surface of NPs. In fact, the formation of spherical shapes is the way the interface energy is minimized during the synthesis of metal NPs.[67, 68] In the present case, however, the lack of miscibility between Ag and Fe is the reason for the formation of new interfaces between amorphous Fe-Ag and crystalline Ag domains inside the same NP, whose energetic cost is comparable to the formation of solid-liquid boundaries.[63] In addition, the diffusivity inside NPs is hampered by the presence of multiple dislocations and boundaries between grains with different crystalline structure, such as fcc silver and amorphous Ag-Fe alloy. The final result is the formation of truffle-like NPs with an intermediate shape between the sphere and the fractal cluster obtained by diffusion limited aggregation of laser-generated nanometric nuclei. From this point of view, the synthesis of Fe-Ag NPs represents an opportunity to “freeze” and study the coalescence step of LASiS. In particular, the truffle-like morphology of Fe-Ag NPs suggests that nuclei temperature is close to the melting point when their coalescence takes place, and that the process is fast enough to run out of thermodynamic equilibrium, where the formation of pure Ag, Fe and iron-oxide phases would be favoured.

Chemical composition of Fe-Ag nanotruffles. The chemical composition of Fe-Ag NPs, evidenced for instance by XPS analysis, is the result of the highly reactive environment present in the plasma plume, containing species from the target and species from the solution, all at high temperature, high pressure and in ionized condition.[32] For instance, the formation of Fe_xAg_y bimetallic clusters has been observed during the pulsed laser irradiation of mixed Fe and Ag powders in gas phase,[69] despite the lack of miscibility of the two metals on the bulk scale. This suggests that the same species can form in liquid solution. In the present case, however, the solution contains solvent molecules and dissolved atmospheric gas such as O_2, CO_2, N_2 and H_2O,[32, 45] hence the plasma plume can acts as an oxidising environment. For instance, noble metals NPs such as Au, Ag and Pt NPs obtained by LASiS in aqueous solutions undergo partial surface oxidation,[32] and laser ablation of pure metal iron in water yields iron oxide NPs.[47, 70] Therefore, in the case of the Fe-Ag system, ablated metal iron atoms can readily react with oxygen in the plasma plume, forming different types of oxides with stoichiometry depending on the local concentration of oxidising species. In any case, at times longer compared to the laser ablation dynamics, metal iron on the surface of Fe-Ag NPs will react with oxygen, whereas iron atoms inside the NPs are protected by the external layer of metallic silver and iron oxide. Importantly, oxidation of iron in coalescing nuclei is also compatible with the observation of Fe-Ag NPs with truffle-like shape, because iron oxide creates metal-oxide interfaces and hampers the diffusion of metal atoms necessary to the formation of rounded nanostructures.

Even with LASiS in ethanol, the yield of Fe-Ag NPs does not reach the 100%, and this can be explained with the asymmetry of the reaction conditions intrinsic in LASiS. LASiS is characterized by the formation of four gradients (temperature, pressure, target species concentration and solution species concentration) steeply varying in time and space.[32] In particular, the concentration of solution species increases by getting far from the ablation site, whereas the concentration of target species increases by approaching the ablation site. The same trend occurs for increasing time after the ablation event. Therefore, the probability of reaction between iron and oxidising solution species is higher at the borders of the plasma plume and for longer times after the ablation event: these are the conditions where the formation of distinct silver and iron NPs are more probable during laser ablation of the Fe-Ag target in ethanol. Hence, it is likely that the yield of Fe-Ag NPs can be further improved by avoiding the presence of oxidising solutes and solvents, such as atmospheric oxygen and water molecules, during the synthesis.

This hypothesis was further substantiated by performing the LASiS of Fe-Ag NPs in a more oxidising environment such as H_2O. In this case, the yield of Fe-Ag NPs collected by applying an external magnetic field is lower than in ethanol (see Figure S6 in E.S.M.). This suggests that, in the stage of nuclei coalescence, the sticking coefficient upon collision of silver nuclei with iron oxide nuclei is lower than between the nuclei of metal silver and metal iron. A similar effect may take place during the nucleation stage, if distinct nuclei of silver and iron oxide form instead of bimetallic silver-iron nuclei. Overall, this is another indication that iron oxidation should be avoided during LASiS to achieve the coexistence of the two immiscible elements in the same NP.

Overall mechanism of formation. Overall, the experimental results agree with the formation of Fe-Ag NPs by the following mechanism (Figure 6):

i) Nucleation: After laser ablation of the target, hot nuclei containing Ag, Fe and mixed Ag and Fe are formed. In water, oxidation of iron occurs with high probability, whereas in ethanol this process is less probable due to the lower concentration of oxidising species.

ii) Coalescence: Hot nuclei coalesce together and quickly cool down, forming solid NP. However, due to the high concentration of defects and dislocations, NPs have the structure of a “melted fractal” aggregate, i.e. of a nanotruffle. At borders of the plasma plume, due to the higher concentration of oxidising species from the solution and lower concentration of target species, there is higher probability that iron is oxidised and a consequent lower probability of sticking with silver nuclei, thus avoiding the coexistence of iron and silver in the same nanostructures.

iii) Passivation: Surface oxidation of NPs takes place by interaction with the hot solution species, prosecuting also at room temperature by interaction with atmospheric oxygen or water molecules, thus creating a passivating layer which protects metal iron inside the particles.

We expect that this mechanism works with all immiscible elements having appreciable sticking coefficients between nuclei or for which the formation of mixed nuclei is possible during the fast ablation dynamics.

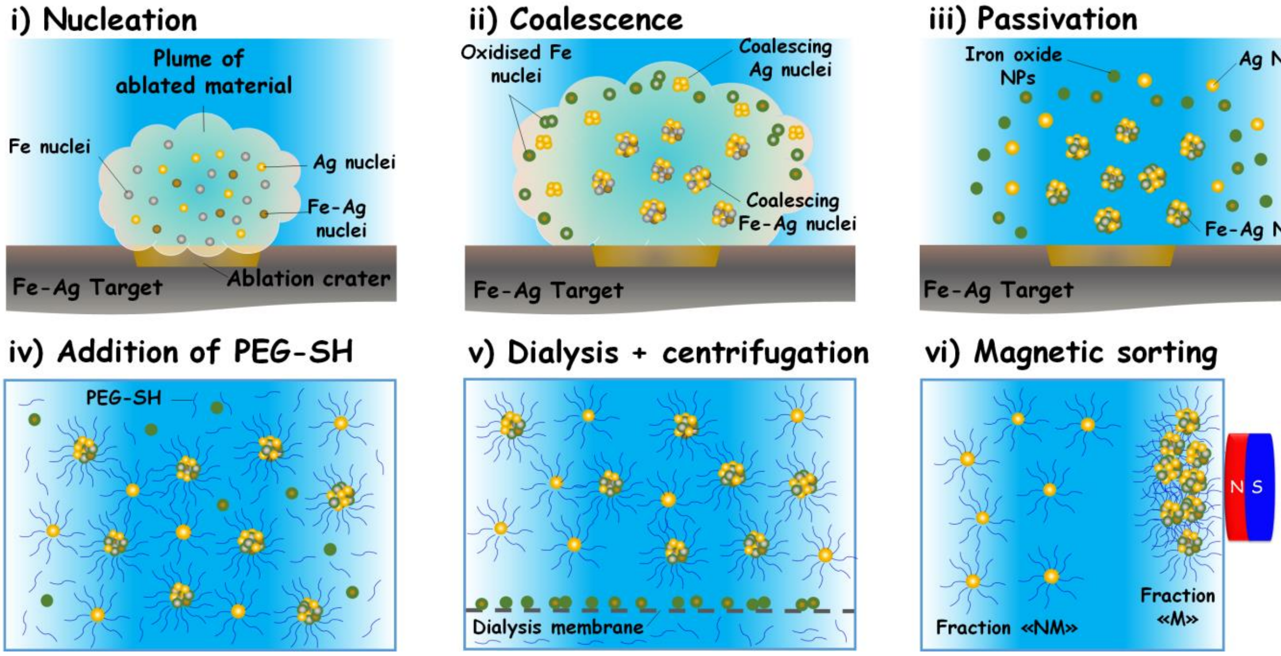

Figure 6. Sketch of the three stages of LASiS permitting the coexistence of the two immiscible elements in the same NPs: i) Nucleation. After laser ablation of the target, hot nuclei containing Ag, Fe and mixed Ag and Fe are formed. In water, oxidation of iron occurs with high probability, whereas in ethanol this process is less probable due to the lower concentration of oxidising species. ii) Coalescence. Hot nuclei coalesce together and quickly cool down, forming solid NP with the structure of a partially melted aggregate. At the borders of the plasma plume, there is higher probability that iron is oxidised and a consequent lower probability of sticking with silver nuclei, thus avoiding the coexistence of iron and silver in the same nanostructures. iii) Passivation. At longer times, surface oxidation of NP occurs by interaction with atmospheric oxygen or water molecules. In the following synthetic steps, thiolated PEG is added and binding with surface Ag atoms takes place (iv), unstabilized NPs and excess PEG are removed by centrifugation with dialysis tubes (v) and, finally, magnetic Fe-Ag NPs are separated from non magnetic ones (vi).

Conclusions

We presented a synthetic strategy for the realization of multifunctional NPs composed by two immiscible elements: iron and silver. The synthesis occurs in one-step and exploits the fast kinetics of nanomaterials formation peculiar of LASiS. The Fe-Ag NPs have a truffle-like structure composed by a scaffold of fcc silver embedding metal iron as dopant indisordered silver-iron alloy domains. The surface of Fe-Ag nanotruffles is partly composed of iron oxide and partly of metal silver, thus allowing the functionalization in one pot with thiolated molecules. Overall, Fe-Ag NPs represent a multifunctional material endowed with magnetic and plasmonic properties, easy surface chemistry and a complete colloidal stability. Such a multifunctionality discloses a wide range of applications and, in particular, we exploited Fe-Ag NPs for the magnetic amplification of SERS signals and of photothermal heating.

Our synthetic approach is of general applicability, promising the preparation in one step of NPs containing all the desired elements. We expect that, in the near future, this procedure will play an important role for the preparation of a wide range of new multifunctional nanostructures which are currently unavailable due to unfavourable thermodynamics.

Experimental Methods.

Synthesis. The laser ablation synthesis in solution (LASiS) was performed using 1064 nm (6 ns, 50 Hz) pulses of a Nd-YAG laser with a fluence of 6.7 J/cm^2. The pulses are focused with a 15 cm lens on a bimetallic target composed of 66at% of Ag and 34at% of Fe (from Mateck) placed at the bottom of a cell containing either distilled water or HPLC grade ethanol (>99.8% pure). The so obtained Fe-Ag NPs dispersion (0.1 mg/mL) was mixed with an aqueous solution containing disodium ethylenediaminetetraacetic acid (EDTA, from Sigma Aldrich, 2 mg/mL) and thiolated polyethyleneglycol (PEG, 0.01 mg/mL) and kept for 60 minutes at 30°C. We used thiolated PEG with molar mass of either 2000, 5000 and 20000 Da from Laysan Bio. Then, the Fe-Ag NPs dispersion was washed multiple times with distilled water by dialysis concentration membranes and finally resuspended in distilled water.

Fe-Ag NPs were magnetically sorted by placing a cylindrical NdFeB magnet (4 mm diameter for 8 mm length) below a 1 cm quartz cuvette containing the NPs dispersion. After 1 day of exposure, the supernatant (i.e. the non magnetic fraction) was separated from the material accumulated on the surface of the magnet (i.e. the magnetic fraction). The magnetic fraction was redispersed in distilled water.

Characterization. UV-visible spectra were recorded with a Varian Cary 5 using quartz cells with a 2 mm optical path. FTIR was performed with a Perkin Elmer 1720X, deposing the dried samples on a KBr window. Z-spectroscopy was performed with a Malvern Zetasizer Nano ZS. ICP-MS measurements were carried out with a Thermo Elemental X7 Series instrument equipped with the PlasmaLab software package. For instrument calibration, standard Fe and Ag solutions were purchased from Spectrascan.

Raman measurements for purposes of structural NPs characterization were recorded with a Renishaw inVia micro-Raman spectrometer on a dried powder of Fe-Ag NPs, using the 633 nm line of an He–Ne laser and 5X, 20X and 50X objectives. Laser power was increased from 1 mW to 13 mW in each analysis, in order to probe the initial iron phase (low power) and check for the formation of hematite (typically observed during high power laser irradiation of crystalline iron oxides),[71] although no peaks ascribable to iron oxides were detected in all cases.

TEM analysis was performed with a FEI Tecnai G2 12 operating at 100 kV and equipped with a TVIPS CCD camera. HRTEM, SAED and EDS analysis were carried out at 300 kV with a JEOL JEM 3010 microscope using a Gatan Multiscan CCD 794 Camera and an X-ray energy dispersive spectrometer (EDS, Oxford Instruments). The samples for TEM analysis were prepared by evaporating NPs suspensions on a copper grid coated with an amorphous carbon holey film.

EDS analysis and line scans were performed with a SEM model Zeiss Sigma VP equipped with a Bruker Quantax 200 detector (window size 30 mm^2) and a Silicon Drift Detector. The Ag L lines and the Fe K lines were considered for line scans and quantitative analysis.

XPS measurements were performed with a modified VG ESCALAB MKII (Vacuum generators, Hastings, England) equipped with a twin (Mg/Al) anode X-ray source, a sputter gun, and a hemispherical electrostatic analyzer with a five channel detector. We used the Al-Kα radiation (1486.6 eV) as an excitation source. Photoemission spectra have been obtained at room temperature using normal emission geometry. Prior to measurements, the samples were degassed overnight in the analysis chamber (pressure lower than 10^{-8} mbar). Samples were obtained by drying a droplet of Fe-Ag NPs dispersion at 40°C on a copper sample holder.

XRD patterns were collected with a Philips diffractometer constituted by an X'Pert vertical goniometer with Bragg–Brentano geometry, a focusing graphite monochromator and a proportional counter with a pulse-height discriminator. Nickel-filtered Cu Kα radiation and a step-by-step technique were used (steps of $2\theta=0.05°$), with collection times of 30 s per step. Line broadening analysis (LBA) was carried out using a previously published method,[72] whereas the Rietveld method for quantitative phase analysis exploited the DBWS9600 computer program written by Sakthivel and Young and modified by Riello et al.[73] The PDF file 000-06-0696 for Fe and 010-87-0597 for Ag were used.

Mossbauer spectroscopy was performed at room temperature using a conventional constant acceleration spectrometer with triangular waveform and a ^{57}Co source (nominal strength 1850 MBq) in a Rh matrix. The hyperfine parameters isomer shift (δ), quadrupole splitting (Δ) or quadrupole shift when magnetic splitting occurred (ε), half linewidth at half maximum ($\Gamma_{1/2}$), expressed in mms^{-1} and the internal magnetic field (B), expressed in Tesla, were obtained by means of standard least-squares minimization techniques. The spectra were fitted to Lorentzian line shapes with the minimum number of sextets and doublets. Isomer shift is quoted relative to α metallic iron at room-temperature.

Fluorescence XAS (X-ray Absorption Spectroscopy) data were collected at GILDA beamline (European Synchrotron Radiation Facility, ESRF, Grenoble, experimenti IHHC-2289) at the

Fe-K edge (7112 eV).[74] A Si(311) double crystal monochromator was used; the harmonic rejection was realised by Pd mirrors, having a cut-off energy of 20 keV, and a 13-element Ge fluorescence detector. The energy calibration has been made by measuring the absorption spectrum of metallic Fe. For the measurements, the colloidal samples have been spotted onto Millipore filters and then cooled down to 100 K, aiming at increasing the EXAFS oscillations. The reproducibility in energy has been assured by measuring simultaneously the XAS spectra of a Fe foil, and for every scan found to be better than 0.1 eV. To obtain a reasonable signal to noise ratio, the integration time was adjusted to give ca. 10^6 counts in the fluorescence channel; in addition, in order to avoid distortions of the spectra, the count rate of each element was kept well below the saturation limit. The metal content were as low as ca. 100 μgcm^{-2}, and therefore self-absorption effects in the fluorescence spectra are in principle negligible. For the XANES analysis the spectra were processed by subtracting the smooth pre-edge background fitted with a straight line. The EXAFS extraction and data analysis were performed by means of the ATHENA and EXCURVE codes, respectively. The number of independent EXAFS points for the fit shown in this work is 11.

The magnetic properties were investigated on the samples in the form of dry powder using a Quantum Design MPMS XL-5 SQUID magnetometer. Zero-field-cooled (ZFC) magnetization curves were measured by cooling samples in zero magnetic field (H) and then by increasing the temperature in an applied field of 5 mT, while field-cooled (FC) curves were recorded by cooling the samples in the same probe field. The field dependence of the magnetization (hysteresis loop) was recorded between ±5 T at T=300 K and 2.5 K. The saturation magnetization (M_S) was derived from a plot of M versus 1/H, extrapolating the M values for $1/H \rightarrow 0$.

Numerical calculations. The Discrete Dipole Approximation (DDA) numerical calculations were performed with the DDSCAT 7.1 code,[75] using more than 10^5 dipoles for each target. The optical absorption spectrum of the nanotruffle was obtained by averaging over 18 different orientations in space. The extinction spectra are computed considering unpolarized incident light. The effect of water solvent has been accounted by setting the refractive index of the non-absorbing matrix n=1.334. The complex dielectric constant of Ag was taken from Palik.[76] We adopted a size-corrected dielectric constant to account for electron scattering at NPs surface, as reported in ref.[35]. The extinction spectra are computed considering unpolarized incident light.

SERS measurements. SERS experiments were performed by mixing 0.5 mL of a 0.2 mg/mL Fe-Ag NPs dispersion with 0.1 mL of a 5 10^{-7} M solution of 4-[(4-

dimethylaminophenyl)phenyl-methyl]-*N*,*N*-dimethylaniline (MG, from Sigma Aldrich). Raman measurements were collected at 633 nm, using a power of 3 mW, a 5X objective and a edge filter. At least three Raman measurements of 10 s each were collected on each sample placed in a 2 mm quartz cells. Fe-Ag NPs were magnetically focused by placing a cylindrical NdFeB magnet (2 mm diameter for 4 mm length) for 2 hours below a quartz cuvette containing the sample.

Photothermal heating measurements. Fe-Ag NPs dispersion was placed in a 2 mm optical path quartz cuvette and irradiated at 785nm with a Renishaw solid state laser model HPNIR (3 mm spot size, 1.12 W/cm^2). A thermal camera model FLIR E5 was used to capture the calibrated digital thermographic infrared images of heated sample.

Electronic Supplementary Material.

Supplementary material is available in the online version of this article.

Acknowledgements

Financial support from University of Padova (PRAT no. CPDA114097/11 and Progetto Strategico STPD11RYPT_001) and MIUR (PRIN MULTINANOITA no. 2010JMAZML_001) is gratefully acknowledged.

References

[1]Lee, D.; Koo, H.; Sun, I.; Ryu, J. H.; Kim, K.; Kwon, I. C. Multifunctional nanoparticles for multimodal imaging and theragnosis. *Chem. Soc. Rev.* **2012**, *41*, 2656-2672

[2]Cheng, Z.; Al Zaki, A.; Hui, J. Z.; Muzykantov, V. R.; Tsourkas, A. Multifunctional nanoparticles: cost versus benefit of adding targeting and imaging capabilities. *Science* **2012**, *338*, 903-910

[3]Liu, K.; Jiang, L. Multifunctional integration: from biological to bio-inspired materials. *Acs Nano* **2011**, *5*, 6786-6790

[4]Sun, Y.; Jiang, L.; Zhong, L.; Jiang, Y.; Chen, X. Towards active plasmonic response devices. *Nano Research* **2015**, *8*, 406-417

[5]Armelles, G.; Cebollada, A.; Garcia-Martin, A.; Gonzalez, M. U. Magnetoplasmonics: Combining Magnetic and Plasmonic Functionalities. *Adv. Opt. Mater.* **2013**, *1*, 2-2

[6]Hao, R.; Xing, R.; Xu, Z.; Hou, Y.; Gao, S.; Sun, S. Synthesis, functionalization, and biomedical applications of multifunctional magnetic nanoparticles. *Adv. Mater.* **2010**, *22*, 2729-2742

[7]Peng, S.; Lei, C.; Ren, Y.; Cook, R. E.; Sun, Y. Plasmonic/magnetic bifunctional nanoparticles. *Angew. Chem. Int. Ed.* **2011**, *50*, 3158-3163

[8]Jin, R.; Nobusada, K. Doping and alloying in atomically precise gold nanoparticles. *Nano Research* **2014**, *7*, 285-300

[9]Shen, J.; Su, J.; Yan, J.; Zhao, B.; Wang, D.; Wang, S.; Li, K.; Liu, M.; He, Y.; Mathur, S. Bimetallic nano-mushrooms with DNA-mediated interior nanogaps for high-efficiency SERS signal amplification. *Nano Research* **2015**, *8*, 731-742

[10]García, S.; Zhang, L.; Piburn, G. W.; Henkelman, G.; Humphrey, S. M. Microwave Synthesis of Classically Immiscible Rhodium–Silver and Rhodium–Gold Alloy Nanoparticles: Highly Active Hydrogenation Catalysts. *ACS Nano* **2014**, *8*, 11512-11521

[11]González‐Díaz, J. B.; García‐Martín, A.; García‐Martín, J. M.; Cebollada, A.; Armelles, G.; Sepúlveda, B.; Alaverdyan, Y.; Käll, M. Plasmonic Au/Co/Au Nanosandwiches with Enhanced Magneto‐optical Activity. *Small* **2008**, *4*, 202-205

[12]Bonanni, V.; Bonetti, S.; Pakizeh, T.; Pirzadeh, Z.; Chen, J.; Nogués, J.; Vavassori, P.; Hillenbrand, R.; Åkerman, J.; Dmitriev, A. Designer magnetoplasmonics with nickel nanoferromagnets. *Nano letters* **2011**, *11*, 5333-5338

[13]Pineider, F.; Campo, G.; Bonanni, V.; de Julián Fernández, C.; Mattei, G.; Caneschi, A.; Gatteschi, D.; Sangregorio, C. Circular magnetoplasmonic modes in gold nanoparticles. *Nano letters* **2013**, *13*, 4785-4789

[14]Suntivich, J.; Xu, Z.; Carlton, C. E.; Kim, J.; Han, B.; Lee, S. W.; Bonnet, N.; Marzari, N.; Allard, L. F.; Gasteiger, H. A.; Hamad-Schifferli, K.; Shao-Horn, Y. Surface Composition Tuning of Au-Pt Bimetallic Nanoparticles for Enhanced Carbon Monoxide and Methanol Electro-oxidation. *J. Am. Chem. Soc.* **2013**, *135*, 7985-7991

[15]Amendola, V.; Scaramuzza, S.; Litti, L.; Meneghetti, M.; Zuccolotto, G.; Rosato, A.; Nicolato, E.; Marzola, P.; Fracasso, G.; Anselmi, C.; Pinto, M.; Colombatti, M. Magneto-Plasmonic Au-Fe Alloy Nanoparticles Designed for Multimodal SERS-MRI-CT Imaging. *Small* **2014**, *10*, 2476-2486

[16]Xu, C.; Wang, B.; Sun, S. Dumbbell-like Au−Fe3O4 nanoparticles for target-specific platin delivery. *J. Am. Chem. Soc.* **2009**, *131*, 4216-4217

[17]Sotiriou, G. A.; Visbal-Onufrak, M. A.; Teleki, A.; Juan, E. J.; Hirt, A. M.; Pratsinis, S. E.; Rinaldi, C. Thermal energy dissipation by SiO2-coated plasmonic-superparamagnetic nanoparticles in alternating magnetic fields. *Chem. Mater.* **2013**, *25*, 4603-4612

[18]Chudasama, B.; Vala, A. K.; Andhariya, N.; Upadhyay, R.; Mehta, R. Enhanced antibacterial activity of bifunctional Fe3O4-Ag core-shell nanostructures. *Nano Research* **2009**, *2*, 955-965

[19]Zhai, Y.; Han, L.; Wang, P.; Li, G.; Ren, W.; Liu, L.; Wang, E.; Dong, S. Superparamagnetic plasmonic nanohybrids: shape-controlled synthesis, TEM-induced

structure evolution, and efficient sunlight-driven inactivation of bacteria. *ACS nano* **2011**, *5*, 8562-8570

[20]Bogani, L.; Cavigli, L.; de Julián Fernández, C.; Mazzoldi, P.; Mattei, G.; Gurioli, M.; Dressel, M.; Gatteschi, D. Photocoercivity of Nano‐Stabilized Au: Fe Superparamagnetic Nanoparticles. *Adv. Mater.* **2010**, *22*, 4054–4058

[21]Sarina, S.; Zhu, H.; Jaatinen, E.; Xiao, Q.; Liu, H.; Jia, J.; Chen, C.; Zhao, J. Enhancing Catalytic Performance of Palladium in Gold and Palladium Alloy Nanoparticles for Organic Synthesis Reactions through Visible Light Irradiation at Ambient Temperatures. *J. Am. Chem. Soc.* **2013**, *135*, 5793-5801

[22]Wang, C.; Yin, H.; Dai, S.; Sun, S. A General Approach to Noble Metal− Metal Oxide Dumbbell Nanoparticles and Their Catalytic Application for CO Oxidation. *Chem. Mater.* **2010**, *22*, 3277-3282

[23]Wang, C.; Chen, J.; Zhou, X.; Li, W.; Liu, Y.; Yue, Q.; Xue, Z.; Li, Y.; Elzatahry, A. A.; Deng, Y. Magnetic yolk-shell structured anatase-based microspheres loaded with Au nanoparticles for heterogeneous catalysis. *Nano Research* **2015**, *8*, 238-245

[24]Araújo, J. E.; Lodeiro, C.; Capelo, J. L.; Rodríguez-González, B.; dos Santos, A. A.; Santos, H. M.; Fernández-Lodeiro, J. Novel nanocomposites based on a strawberry-like gold-coated magnetite (Fe@ Au) for protein separation in multiple myeloma serum samples. *Nano Research* **2015**, *8*, 1189-1198

[25]Lou, L.; Yu, K.; Zhang, Z.; Huang, R.; Zhu, J.; Wang, Y.; Zhu, Z. Dual-mode protein detection based on Fe3O4-Au hybrid nanoparticles. *Nano Research* **2012**, *5*, 272-282

[26]Kadasala, N. R.; Wei, A. Trace detection of tetrabromobisphenol A by SERS with DMAP-modified magnetic gold nanoclusters. *Nanoscale* **2015**, *7*, 10931-10935

[27]La Porta, A.; Sánchez-Iglesias, A.; Altantzis, T.; Bals, S.; Grzelczak, M.; Liz-Marzán, L. M. Multifunctional self-assembled composite colloids and their application to SERS detection. *Nanoscale* **2015**, *7*, 10377-10381

[28]Ferrando, R.; Jellinek, J.; Johnston, R. L. Nanoalloys: from theory to applications of alloy clusters and nanoparticles. *Chem. Rev.* **2008**, *108*, 845-910

[29]LaGrow, A. P.; Knudsen, K. R.; AlYami, N. M.; Anjum, D. H.; Bakr, O. M. The Effect of Precursor Ligands and Oxidation State in the Synthesis of Bimetallic Nano-Alloys. *Chem. Mater.* **2015**, *27*, 4134-4141

[30]Lin, F.; Chen, W.; Liao, Y.; Doong, R.; Li, Y. Effective approach for the synthesis of monodisperse magnetic nanocrystals and M-Fe3O4 (M= Ag, Au, Pt, Pd) heterostructures. *Nano Research* **2011**, *4*, 1223-1232

[31]Zeng, H.; Du, X.; Singh, S. C.; Kulinich, S. A.; Yang, S.; He, J.; Cai, W. Nanomaterials via laser ablation/irradiation in liquid: a review. *Adv. Funct. Mater.* **2012**, *22*, 1333-1353

[32]Amendola, V.; Meneghetti, M. What controls the composition and the structure of nanomaterials generated by laser ablation in liquid solution? *Phys.Chem.Chem.Phys.* **2013**, *15*, 3027-3046

[33]Amendola, V.; Meneghetti, M.; Bakr, O. M.; Riello, P.; Polizzi, S.; Fiameni, S.; Dalaver, H.; Arosio, P.; Orlando, T.; de Julian Fernandez, C.; Pineider, F.; Sangregorio, C.; Lascialfari, A. Coexistence of magnetic and plasmonic properties in Au89Fe11 nanoalloys. *Nanoscale* **2013**, *5*, 5611-5619

[34]Amendola, V.; Scaramuzza, S.; Agnoli, S.; Polizzi, S.; Meneghetti, M. Strong dependence of surface plasmon resonance and surface enhanced Raman scattering on the composition of Au-Fe nanoalloys. *Nanoscale* **2014**, *6*, 1423-1433

[35]Amendola, V.; Bakr, O. M.; Stellacci, F. A study of the surface plasmon resonance of silver nanoparticles by the discrete dipole approximation method: effect of shape, size, structure, and assembly. *Plasmonics* **2010**, *5*, 85-97

[36]Swartzendruber, L. The Ag− Fe (Silver-Iron) system. *J. Phas. Equil.* **1984**, *5*, 560-564

[37]Wan, H.; Tsoukatos, A.; Hadjipanayis, G.; Li, Z.; Liu, J. Direct evidence of phase separation in as-deposited Fe (Co)-Ag films with giant magnetoresistance. *Phys. Rev. B* **1994**, *49*, 1524

[38]Kataoka, N.; Sumiyama, K.; Nakamura, Y. Magnetic properties of high-concentration Fe-Ag alloys produced by vapour quenching. *J. Phys. F: Met. Phys.* **1985**, *15*, 1405

[39]Kataoka, N.; Sumiyama, K.; Nakamura, Y. Nonequilibrium crystalline Fe-Ag alloys vapour-quenched on liquid-nitrogen-cooled substrates. *J. Phys. F: Met. Phys.* **1988**, *18*, 1049

[40]Shi, Z.; Wang, T.; Lin, H.; Wang, X.; Ding, J.; Shao, M. Excellent surface-enhanced Raman scattering (SERS) based on AgFeO2 semiconductor nanoparticles. *Nanoscale* **2013**, *5*, 10029-10033

[41]Han, X. X.; Schmidt, A. M.; Marten, G.; Fischer, A.; Weidinger, I. M.; Hildebrandt, P. Magnetic Ag Hybrid Nanoparticles for Surface Enhanced Resonance Raman Spectroscopic Detection and Decontamination of Small Toxic Molecules. *ACS Nano* **2013**, *7*, 3212-3220

[42]Mahmoudi, M.; Serpooshan, V. Silver-coated engineered magnetic nanoparticles are promising for the success in the fight against antibacterial resistance threat. *ACS nano* **2012**, *6*, 2656-2664

[43]Murphy, C. J. Sustainability as an emerging design criterion in nanoparticle synthesis and applications. *J. Mater. Chem.* **2008**, *18*, 2173-2176

[44]Compagnini, G.; Scalisi, A. A.; Puglisi, O. Ablation of noble metals in liquids: a method to obtain nanoparticles in a thin polymeric film. *Phys.Chem.Chem.Phys.* **2002**, *4*, 2787-2791

[45]Amendola, V.; Riello, P.; Meneghetti, M. Magnetic Nanoparticles of Iron Carbide, Iron Oxide, Iron@ Iron Oxide, and Metal Iron Synthesized by Laser Ablation in Organic Solvents. *J Phys. Chem. C* **2011**, *115*, 5140–5146

[46]Amendola, V.; Polizzi, S.; Meneghetti, M. Free Silver Nanoparticles Synthesized by Laser Ablation in Organic Solvents and Their Easy Functionalization. *Langmuir* **2007**, *23*, 6766-6770

[47]Amendola, V.; Riello, P.; Polizzi, S.; Fiameni, S.; Innocenti, C.; Sangregorio, C.; Meneghetti, M. Magnetic iron oxide nanoparticles with tunable size and free surface obtained via a “green” approach based on laser irradiation in water. *J. Mater. Chem.* **2011**, *21*, 18665-18673

[48]Santillán, J. M.; van Raap, Marcela B Fernández; Zélis, P. M.; Coral, D.; Muraca, D.; Schinca, D. C.; Scaffardi, L. B. Ag nanoparticles formed by femtosecond pulse laser ablation in water: self-assembled fractal structures. *J. Nanop. Res.* **2015**, *17*, 1-13

[49]Santillán, J.; Scaffardi, L.; Schinca, D. Quantitative optical extinction-based parametric method for sizing a single core–shell Ag–Ag2O nanoparticle. *J. Phys. D* **2011**, *44*, 105104

[50]Lim, J.; Majetich, S. A. Composite magnetic–plasmonic nanoparticles for biomedicine: Manipulation and imaging. *Nano Today* **2013**, *8*, 98-113

[51]Scaramuzza, S.; Agnoli, S.; Amendola, V. Metastable alloy nanoparticles, metal-oxide nanocrescents and nanoshells generated by laser ablation in liquid solution: influence of the chemical environment on structure and composition. *Phys. Chem. Chem. Phys.* **2015**

[52]Maenosono, S.; Lee, J.; Dao, A. T. N.; Mott, D. Peak shape analysis of Ag 3d core ‐ level X ‐ ray photoelectron spectra of Au@ Ag core ‐ shell nanoparticles using an asymmetric Gaussian‐Lorentzian mixed function. *Surf. Interface Anal.* **2012**, *44*, 1611-1614

[53]Grosvenor, A.; Kobe, B.; Biesinger, M.; McIntyre, N. Investigation of multiplet splitting of Fe 2p XPS spectra and bonding in iron compounds. *Surf. Interface Anal.* **2004**, *36*, 1564-1574

[54]Naitabdi, A.; Ono, L.; Behafarid, F.; Cuenya, B. R. Thermal Stability and Segregation Processes in Self-Assembled Size-Selected Au x Fe1-x Nanoparticles Deposited on TiO2 (110): Composition Effects. *J. Phys. Chem. C* **2009**, *113*, 1433-1446

[55]Santhi, K.; Thirumal, E.; Karthick, S.; Kim, H.; Narayanan, V.; Stephen, A. Structural and magnetic investigations on metastable Ag–Fe nanophase alloy. *J. Alloys Compounds* **2013**, *557*, 172-178

[56]Lebugle, A.; Axelsson, U.; Nyholm, R.; Mårtensson, N. Experimental L and M core level binding energies for the metals 22Ti to 30Zn. *Phys. Scripta* **1981**, *23*, 825

[57]Alonso, J.; Fdez-Gubieda, M.; Svalov, A.; Meneghini, C.; Orue, I. Effects of thermal annealing on the magnetic interactions in nanogranular Fe–Ag thin films. *J. Alloys Compounds* **2012**, *536*, S271-S276

[58]Wang, J.; Xiao, G. Transition-metal granular solids: Microstructure, magnetic properties, and giant magnetoresistance. *Phys. Rev. B* **1994**, *49*, 3982

[59]Binns, C.; Maher, M.; Pankhurst, Q.; Kechrakos, D.; Trohidou, K. Magnetic behavior of nanostructured films assembled from preformed Fe clusters embedded in Ag. *Phys. Rev. B* **2002**, *66*, 184413

[60]Malviya, K. D.; Chattopadhyay, K. Synthesis and Mechanism of Composition and Size Dependent Morphology Selection in Nanoparticles of Ag-Cu Alloys Processed by Laser Ablation Under Liquid Medium. *J. Phys. Chem. C* **2014**, *118*, 13228-13237

[61]Yudanov, I. V.; Metzner, M.; Genest, A.; Rösch, N. Size-dependence of adsorption properties of metal nanoparticles: a density functional study on palladium nanoclusters. *J. Phys. Chem. C* **2008**, *112*, 20269-20275

[62]Panizon, E.; Bochicchio, D.; Rossi, G.; Ferrando, R. Tuning the structure of nanoparticles by small concentrations of impurities. *Chem. Mater.* **2014**

[63]Peng, Y.; Wang, F.; Wang, Z.; Alsayed, A. M.; Zhang, Z.; Yodh, A. G.; Han, Y. Two-step nucleation mechanism in solid–solid phase transitions. *Nat. Mater.* **2015**, *14*, 101-108

[64]Wagener, P.; Ibrahimkutty, S.; Menzel, A.; Plech, A.; Barcikowski, S. Dynamics of silver nanoparticle formation and agglomeration inside the cavitation bubble after pulsed laser ablation in liquid. *Phys.Chem.Chem.Phys.* **2013**, *15*, 3068-3074

[65]Compagnini, G.; Messina, E.; Puglisi, O.; Nicolosi, V. Laser synthesis of Au/Ag colloidal nano-alloys: Optical properties, structure and composition. *Appl. Surf. Sci.* **2007**, *254*, 1007-1011

[66]Tiedemann, D.; Taylor, U.; Rehbock, C.; Jakobi, J.; Klein, S.; Kues, W. A.; Barcikowski, S.; Rath, D. Reprotoxicity of gold, silver, and gold–silver alloy nanoparticles on mammalian gametes. *Analyst* **2014**, *139*, 931-942

[67]Capelo, R. G.; Leppert, L.; Albuquerque, R. Q. d. On the Concept of Localized Atomic Mobility: Unraveling Properties of Nanoparticles. *J. Phys. Chem. C* **2014**, *118*, 21647-21654

[68]Link, S.; Burda, C.; Nikoobakht, B.; El-Sayed, M. A. Laser-Induced Shape Changes of Colloidal Gold Nanorods Using Femtosecond and Nanosecond Laser Pulses. *J Phys Chem B* **2000**, *104*, 6152-6163

[69]Andrews, M. P.; O'Brien, S. C. Gas-phase" molecular alloys" of bulk immiscible elements: iron-silver (FexAgy). *J. Phys. Chem.* **1992**, *96*, 8233-8241

[70]Amendola, V.; Meneghetti, M.; Granozzi, G.; Agnoli, S.; Polizzi, S.; Riello, P.; Boscaini, A.; Anselmi, C.; Fracasso, G.; Colombatti, M. Top-down synthesis of multifunctional iron oxide nanoparticles for macrophage labelling and manipulation. *J. Mater. Chem.* **2011**, *21*, 3803-3813

[71]McCarty, K. F.; Monti, M.; Nie, S.; Siegel, D. A.; Starodub, E.; El Gabaly, F.; McDaniel, A. H.; Shavorskiy, A.; Tyliszczak, T.; Bluhm, H. Oxidation of Magnetite (100) to Hematite Observed by In-situ Spectroscopy and Microscopy. *J. Phys. Chem. C* **2014**, *118*, 19768-19777

[72]Enzo, S.; Polizzi, S.; Benedetti, A. Applications of fitting techniques to the Warren-Averbach method for X-ray line broadening analysis. *Z. Kristallogr.* **1985**, *170*, 275-287

[73]Riello, P.; Canton, P.; Fagherazzi, G. Quantitative Phase Analysis in Semicrystalline Materials Using the Rietveld Method. *J. Appl. Crystallogr.* **1998**, *31*, 78-82

[74]D'Acapito, F.; Colonna, S.; Pascarelli, S.; Antonioli, G.; Balerna, A.; Bazzini, A.; Boscherini, F.; Campolungo, F.; Chini, G.; Dalba, G.; Davoli, I.; Fornasini, P.; Graziola, R.; Licheri, G.; Meneghini, C.; Rocca, F.; Sangiorgio, L.; Sciarra, V.; Tullio, V.; Mobilio, S. *ESRF Newsletter* **1998**, *30*, 42-44

[75]Draine, B.; Flatau, P. User Guide to the Discrete Dipole Approximation Code DDSCAT 7.1, 2010./h ttp. *arxiv.org/abs/1002.1505v1 S*

[76]Palik, E. D. *Handbook of Optical Constants of Solids;* Academic Press: 1985;